Nano World Journal

https://doi.org/10.17756/nwj.2023-s3-054

Research Article

Open Access

Machine Learning-based Investigation of Wear and Frictional Behavior in Graphite-reinforced Aluminum Nanocomposites

Sathishkumar Arumugam[1], Sachin Kumar[2], Pramod Sridhara[3], Srinivasan Raju[4*], Ashwin Prabhu Gnanasekaran[5], Nanthakumar Sivasamy[6] and Thangarajan Sivasankaran Senthilkumar[7]

[1]*Department of Electronics and Communication Engineering, Erode Sengunthar Engineering College, Erode, Tamil Nadu, India*

[2]*Department of Mechanical Engineering, University Institute of Engineering and Technology, Maharshi Dayanand University, Rohtak, Haryana, India*

[3]*Department of Mathematics, Nitte Meenakshi Institute of Technology, Bangalore, Karnataka, India*

[4]*Department of Mechanical Engineering, Sri Krishna College of Technology, Coimbatore, Tamil Nadu, India*

[5]*Department of Mechanical Engineering, St. Joseph's College of Engineering, Chennai, Tamil Nadu, India*

[6]*Department of Mechanical Engineering, PSG Institute of Technology and Applied Research, Coimbatore, Tamil Nadu, India*

[7]*Department of Mechanical Engineering, K. Ramakrishnan College of Technology, Tiruchirappalli, Tamil Nadu, India*

***Correspondence to:**
Srinivasan Raju
Department of Mechanical Engineering,
Sri Krishna College of Technology,
Coimbatore, Tamil Nadu, India.
E-mail: vlbsrini@gmail.com

Received: July 28, 2023
Accepted: October 09, 2023
Published: October 11, 2023

Citation: Arumugam S, Kumar S, Sridhara P, Raju S, Gnanasekaran AP, et al. 2023. Machine Learning-based Investigation of Wear and Frictional Behavior in Graphite-reinforced Aluminum Nanocomposites. *NanoWorld J* 9(S3): S278-S287.

Copyright: © 2023 Arumugam et al. This is an Open Access article distributed under the terms of the Creative Commons Attribution 4.0 International License (CCBY) (http://creativecommons.org/licenses/by/4.0/) which permits commercial use, including reproduction, adaptation, and distribution of the article provided the original author and source are credited.

Published by United Scientific Group

Abstract

The researcher used a cell segmentation technique in conjunction with other image analysis methods to quantitatively retrieve and compute the cellular microstructural structures in a sub-grain size of silicon carbide (SiC)-reinforced AA2219 made by powderfusion bed (size 0.5 - 1μm). Over 83 geometric features were retrieved and statistically analyzed using ML (Machine learning) techniques to examine the structure-property relationships in SiC-reinforced AlSi20Mg nanocomposites. These sub-grain cellular microstructure properties were utilized to develop hardness and relative mass density analytical models. Using principal component analysis (PCA), authors could narrow down the three variables.While all of the AlSi20Mg nanocomposite samples had identical Al-Si eutectic microstructures, the mechanical properties, such as hardness and relative mass density, varied widely depending on the laser parameters used to create them. Extra Tress regression models that attempted to predict hardness had a close error rate of 2.47%. Usinga regression model based on Decision Trees, authors could predict relative mass density towithin 0.42 standard deviations. The established models are shown to be capable of predicting the relative hardness and relative mass density of AlSi20Mg nanocomposites. The structure identified in this study has applications for controlling the mechanical properties of PFB (powder fusion beds) and could be applied to other additively manufactured alloys and composites.

Keywords

AlSi20Mg, Machine learning, Silicon carbide, Powder fusion bed, Microstructure, Segmentation

Introduction

Many studies have investigated the feasibility of using AlSi20Mg, and eutectic Al-Si alloy, in PFB [1, 2]. AlSi20Mg is a popular casting alloy for challenging structures because of its higher strength, solidity, and well-dynamic characteristics under heavy loads. Researcher can customize the treatment of machined, spark-eroded, welded, shot-peened, coated, and polished AlSi20Mg components [3]. Due to cooling-induced recrystallization, the PFB of AlSi20Mg can yield small equiaxed grains with a delicate pseudo-eutectic cellular microstructure. AlSi20Mg melt of differentlengths formed into columnar grains [4]. Unique properties result from the alloy's unusual near-eutectic Al-Si microstructure.

Modifying process parameters often results in a porous-free, dense material with a high microhardness during PFB manufacturing of alloys (such as laser power and scan speed). PFB AlSi20Mg alloy components have their vertical surface roughness investigated to better understand this factor [5]. A comparatively higher density of track energy delivered to the contours is required to produce a flat, even surface. Hasan et al. [6] analyzed the plastic and fracture performance of AlSi20Mg samples generated via casting and PFB. Results showed that compared to PFB-produced AlSi20Mg, cast samples exhibited lower yield strength (YS) and higher ultimate tensile strength (UTS). With a mean radius of 10.7 m, the voids in the PFB-produced alloy are substantially smaller and more circular. Yang et al. [7] found that the ductile strength, YS, UTS, and modulus of AlSi20Mg PFB-produced samples correlated with their porosity using a linear fit, a defect exposure technique, and a problematic limited strain [8]. The correlation between flexibility and porosity was experimentally established. The research demonstrates that macro characteristics like porosity and roughness produced by PFB on AlSi20Mg samplesare insufficient to infer mechanical parameters, including YS, UTS, and hardness [9].

Regarding the microstructural–property links, other microstructure indicators shouldbe investigated. AlSi20Mg's mechanical behavior was discovered to be correlated with its sub-grain cellular structure. Modifying the specimen hardness by altering the energy input and heat treatment is possible due to the microscopic cellular-dendritic solidification structure variation [10]. To define the connection between the cellular structure of AlSi20Mg at the sub-grain level and the material mechanical properties, Yang and Özel [11] derived two distinct morphological indices, the dimension-scale index, and form index, from SEM (Scanning electron microscope) pictures. Alterations in sub-grain cell size and cell boundary morphology were shown to have a significant impact on the mechanical characteristics of PFB-produced AlSi20Mg. However, there hasn't been enough study dedicated to developing a more precise depiction of the sub-grain cellular structure. Composites comprising metal matrices and reinforcing phases show enhanced dynamic behavior and mechanical characteristics [12]. Paulson et al. [13] discovered, micro/nano metal matric composite created with PFB can offer benefits over unreinforced materials.

As a very effective data-driven modeling tool, ML has been the subject of substantial research in the fields of intelligent manufacturing processes and quality control, and additive manufacturing behavior forecast. Extreme gradient boosting and long short-term memory (LSTM) were used by Doyle et al. [14] in directed energy deposition to predict the melt pool temperature. It was found that in settings with moderate temperature fluctuations, LSTM outperforms excessive gradient boosting. Comparing LSTM to XGBoost, researcher will notice that the latter has far better computing efficiency. A hybrid Bayesian network was employed to forecast the quality of 316 L components made using selective laser melting [15]. Good prediction accuracy was foundwhen only four machine parts were used for training, originating from a device that was left out of the practicing set. SLM requires a large amount of training data, so additional process features may be incorporated into the prediction. Yu et al. [16] explored the potential of the machine learning instruments MIPHA and rMIPHA for use in analyzing steel properties based on 2D and 3D microstructure characteristics like area proportion, obliqueness, hardness, ferret's span or angular position, count proportion, volume proportion, area of the surface, Gauss curve, sphericity, sort, etc. Reverse engineering using MIPHA allowed us to examine microstructures that provide the stress-strain curvature, tensile strength, and overall elongation. The complex amorphous structure of metallic glass was defined by Suzuki et al. [17], employing a single rigidity-oriented structural characteristic associated with the pair distributional role of distinct atoms via a weight function. Vibrational, diffusional, elastic, and plastic relaxation responses are all shown to correlatewith the underlying structure [18]. However, PFB-made AlSi20Mg-based composites are still in their infancy in terms of a high-fidelity data-driven model for the microstructural-mechanical characteristics couplings [19].

This study aims to fill the knowledge gap concerning PFB-created AlSi20Mg nanocomposites by elucidating the relationships between the nanocomposites' sub-grain microstructure and their mechanical properties, investigating the impact of laser factors on melt pool geometry and sub-granular texture. The nanocomposites porosity and microstructure are affected by the laser parameters used to create them. The mechanical characteristics of AlSi20Mg nanocomposites were predicted using ML and microstructural texture data. This analysis aims to develop a methodology for characterizing and estimating the correlation between the variation in microstructural texture generated by changing laser parameters and the resulting changes in the hardness than the relative density of SiCs/AlSi20Mg composites. The developed model can be employed for optimizing processes and designing new materials. The principal component analysis employed here is amenable to future adaptation for use with different alloys and was used to aid in the discovery of the nanocomposites tiny microstructure. It elucidated the connection between the sub-grain cellular microstructure and mechanical characteristics of PFB-produced SiC-reinforced AA2219 as an outcome of rapid cooling.

Materials and Method

Processing of material and PFB

Commercial gas-atomized AlSi20Mg powder (particle size range: 30 - 115 μm) and untreated SiC (outer diameter: 3 - 15 nm, span: 20 - 40 μm) were employedas raw materials for SiC (SiC 0.5 wt.%) - strengthened AA2219. SiC was consistently coatedon the surfaces of AlSi20Mg particles using an XQM-4 planetary ball mill. There were asmany steel balls as there were powders, and the mixture was stored in stainless steel bowls.The rotating speed was set to 200 rpm, and the milling time was 4 h. Every 15 minof milling was followed by a 5-min break to prevent the powder combination from overheating. The powder was dried in a vacuum chamber at 80 °C for 4 h

The PFB processing was performed with an ytterbium fiber laser that peaked at 550 W, had a size of 95 m, and

maintained a wavelength of 1080 nm on a commercial SLM machine with a 275 mm x 275 mm x 340 mm build volume. Table 1 shows that this study tested 16 samples produced using a variant scan speed (1.9 - 2.5 m/s) and laser power (360 - 460 W). Previous reports [14] detailed the comprehensive material characterization and mechanical testing findings of SiCs/AlSi20Mg nanocomposites. In our earlier research, nanocomposites with SiC reinforcement have superior mechanical properties to AlSi20Mg without SiC reinforcement, with yield strengths increasing by more than 10%.

Table 1: The laser factors, hardness measurements, and relative density of PFB-made SiC-reinforced AA2219.

S. No.	Laser power (W)	Laser scan speed (m/s)	Hardness (HV)	Relative mass density (%)
1	460	2.5	128.60	97.21
2	460	2.3	125.35	98.86
3	460	2.1	126.31	99.78
4	460	1.9	125.63	99.18
5	418.4	2.5	120.72	96.54
6	418.4	2.3	123.91	97.46
7	418.4	2.1	124.26	99.02
8	418.4	1.9	124.31	98.63
9	385.6	2.5	98.62	94.83
10	385.6	2.3	104.81	96.24
11	385.6	2.1	123.23	99.45
12	385.6	1.9	124.12	99.23
13	360	2.5	101.63	93.12
14	360	2.3	121.87	94.26
15	360	2.1	124.36	97.35
16	360	1.9	121.12	95.86

This study aims to create a high-fidelity experimented-computerized structure for characterizing the cell framework of SiCs/AlSi20Mg composites, with the goal of correlating the sub-grain microstructural with their mechanical characteristics.

The relative mass density of SiCs/AlSi20Mg nanocomposites is determined employing Archimedes' principle of density. With optical pictures and Image approach, researcher could also calculate the areal density of micropores and identify voids within them [20]. These two density measurements yield comparable results for various samples.A Vickers hardness tester with a weight of 10 kg and a period of 5 s was utilized to conducthardness testing [21]. The sub-grain cellular microstructure was captured by SEM at 13,000 and 26,000 magnification. Optical microscopy was utilized to analyze the microstructures of the samples and the morphology of the melt pool [22].

Image processing for cellular structures

Figure 1 depicts various melt pool microstructures of the as-built SiCs/AlSi20Mg nanocomposites. The surface morphology of the melt pool, which has a roughly 45° texture, and the laser scan pattern is indicated in figure 1a. Figure 1b depicts the cross-sectional morphology of a melt pool, showing melt layers formed parallel to the build direction and devoid of micro-porosity. It is challenging to quantitatively differentiate themelt pool shape of variant laser factors due to the overlapping melt pools on the top surface.According to our previous research, it is impossible to relate the form of melt pools to theirmechanical characteristics like hardness and relative mass density because of the microporous nature of the nonuniformity in the macro-scale microstructure.

The sub-grain cellular eutectic structure of the SiCs/AlSi20Mg nanocomposite specimens was processed and described using SEM imaging to solve the problem of linking the microstructure to mechanical properties (Figure 2). To the contrary, SiCs/AlSi20Mg nanocomposites show a eutectic and sub-cell. Aluminum-silicon microstructural in a planevertical to the direction of construction, as determined by sub-grain analysis [23]. For specimen 1 and 12, the size and shape of the sub-grain cellular microstructure aresignificantly affected by the laser settings. Most sub-cells in the temperate zone fall withinthe 0.5 - 1 µm size range, while cells in the coarse region are 1 - 2 µm in size. For the fine sub-grain region, a network of Si precipitates surrounds a dark a-Al matrix [24]. Visible inthe hazier parts of the heat-affected zone (HAZ) are Si precipitates that have formed morerandomly. The delicate sub-grain phase predominates over the HAZ/coarse sub-grain zone.Therefore, this research aimed to examine how tiny sub-grain texture features in SiCs/AlSi20Mg nanocomposites affected their hardness and relative density. This work considers that six photos per sample adequately describe the geometrical properties in thefine cell zone because more than 2,000 cells may be recognized for each image.

Bulk characteristics, such as porosity, and the particular Al-Si eutectic microstructureof the nanocomposites are linked to

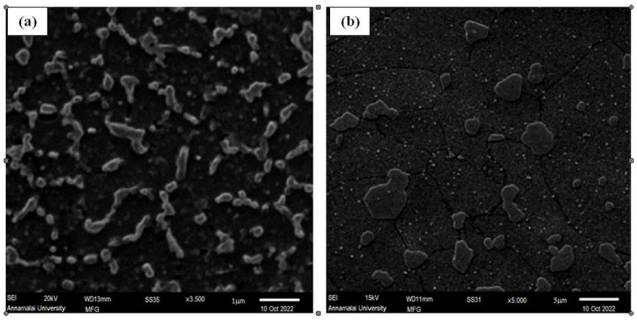


Figure 1: Microstructure of SiC/AlSi20Mg nanocomposite indicates melted pool morphologies: **(a)** Microscope in the dark area, top surface and **(b)** the segment across the structure displaying melt layers with no visible micro-pores or flaws.

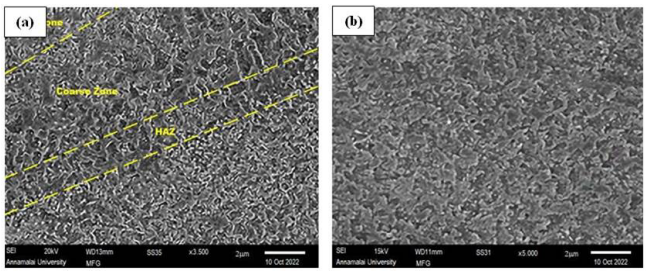


Figure 2: (a) Specimen No. 1 with a 460 W at 2.5 m/s shows fine and coarse cell microstructural image and **(b)** while specimen No. 12 with a 360 W at 2.1 m/s shows a non-uniform fine cellular dispersal both in a plane vertical to the shape direction.

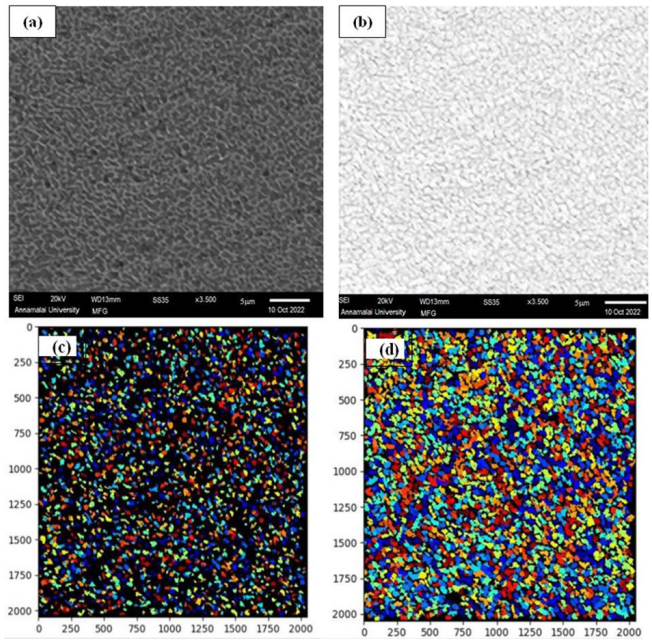


Figure 3: SEM picture of the ultra-fine cell region in **(a)** SiC/AlSi20Mg, **(b)** the inverse gray photograph, **(c)** a cellular nucleus plot obtained through b and d a segmented cellular map displaying a higher fidelity depiction of the fine cellular zone cell form as well as size.

their mechanical elements, such as surface hardness. Software was used to segment the cells in the SEM picture and extract their geometric properties. Figure 3d shows that high-quality cell segmentation characteristics require multiple image processing steps:

- As a means of enhancing the contrast, the original SEM image was converted from color to black and white;
- Set the size of the cell nuclei to between 0.15 and 0.5 m, and then use the Otsu thresholds to isolate.
- The SEM image shows a close-up of the nuclei of the various cellular components. The Otsu method minimizes the variation between the two groups of pixels (foreground (f) and background (b)) using the equation. This allows it to be used to determine the optimal threshold for distinguishing between the two (1),

$$T_{opt} = \arg m\left\{\frac{P(T)\left[1-P(T)\right]\left[m_F(T)m_b(T)\right]^2}{P(T)\sigma_f^2(T)+\left[1+P(T)\right]\sigma_b^2(T)}\right\} \quad (1)$$

Where P(*T*) is probability function, $\sigma_f^2(T)$ and $\sigma_b^2(T)$ are foreground and background of class variances, $m_f(T)$ and $m_b(T)$ are class means. This method produces excellent results when the pixel counts in adjacent cells are similar, as shown in figure 3c.

- Figure 3d displays the calculations used to determine cell shape and coordination using individual nuclei data. The boundary between adjacent cellsis defined using the propagation technique. The final threshold is determined by determining the value of the least cross-entropy among the foreground and background circulations (Equation 2).

$$T_{opt} = \arg m\left[\sum_{g=0}^{T} gp(g)\log\frac{g}{m_F(T)} + \sum_{g=T+1}^{G} gp(g)\log\frac{g}{m_b(T)}\right] \quad (2)$$

Where $= \sum_{g\le T} m_f(T)$ and $\sum_{g\ge} g = \sum_{g\ge T} m_b(T)$

In figure 3a, for instance, there were 2,466 cells counted. Each cell's geometricfeatures were determined. Researcher retrieved and computed a total of 83 coordinate-independent characteristics for each cell. The following are descriptions of various essential qualities among those employed in this investigation:

A cell's size is measured in terms of its perimeter, which is the distance around its perimeter. Specifically, the eccentricity of an ellipse is the ratio of its focus distance to itsmaximum axis length. Its values range from zero to one. The cell extent is the fraction of its bounding box. The degree of solidity is defined as the fraction of the convex hull withinthe cell. One can define a tight circle as one that is filled. The irregular or missing cells have a more significant value than 1. Distance from one point inside an entity to the nearestpoint outside the cell is its average radius [25]. An accurate description of the geometry and shape of a cell required multiple seconds. First, a circle is defined by finding the location of the cell center of mass. Using this method, researchers determined a cell Zernikemoments Z_{nl}.

$$Z_{nl} = \frac{n+1}{n}\sum_x\sum_y V_{nl}^*(x,y)f(x,y) \quad (3)$$

Where $x^2 + y^2 \le 1$, $0 \le l \le n, n - l$ is even, $V_{nl}^*(x,y)$ complex conjugation, $V_{n1}(x,y)$ is definite as

$$Vn1(x,y) = \sum_{m=0}^{(n-l)/2}(-1)^m\frac{(n-m)!}{m!\left[\frac{(n-2m+l)}{2}\right]!\left[\frac{(n-2m+l)}{2}\right]!}-\left(x^2+y^2\right)^{(n/2)-m_e^{il\theta}} \quad (4)$$

Where $0 \le l \le n$,

$n - l$ even

$\theta = \tan^{-1}(y/x)$, and $i = \sqrt{-1}$.

This investigation computed Zernike polynomials of orders 0 through 9, along with a total of 30 characteristics. This section provides a quick overview of the other significant components. A cell spatial moment features is the sum of many weighted averages of its dimensions, orientations, and distances. As the cell's centroid is used as the reference point, central moment features are insensitive to the spatial context in which the cell is located. Scale-invariant normalization of moment features removes the impact of cell size on previously normalized features [26]. In contrast to other moment features of a cell, the Humoment features are invariant under changes in the cell's position, size, and orientation. The form of a cell can be best described by looking at it at various times.

Figure 4 illustrates a flowchart of the proposed microstructure-property linkage framework for SiC/AlSi20Mg nanocomposites using PFB. The framework considers cell segmentation and machine learning support. By processing and segmenting SEM images,researcher can examine the microstructure and determine where the Si-

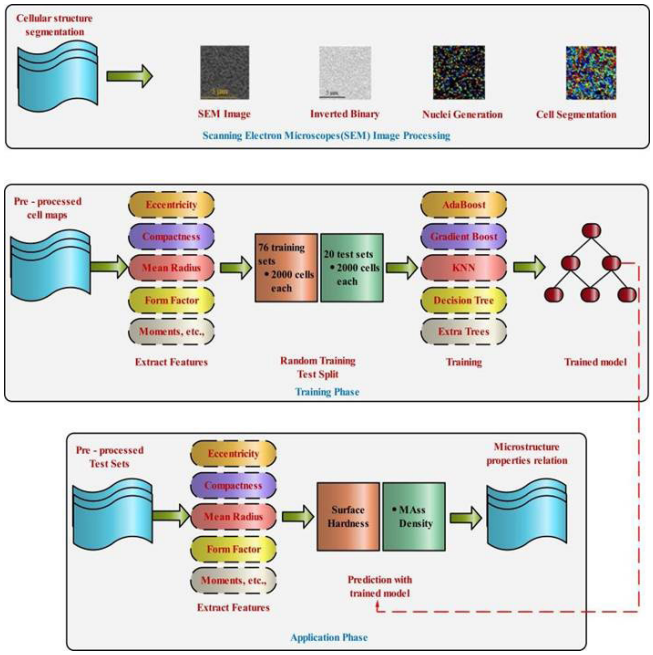


Figure 4: An overview of the suggested processing framework pipeline for microstructure-property links in AlSi20Mg nanocomposites synthesized via LBPF.

rich phase and aluminum phase are located within individual cells [12]. Images with a broken Si-rich stage were processed by joining dashed dots to create whole cells. The following picture isformed by associating the pixels inside a cell with the aluminum phase and the pixels outside with the Si-rich stage. Next, researcher presented data from both the Si-rich and aluminum phases by extracting and calculating morphological features for each cell. In the training phase, it was demonstrated how 76 sample SEM images were chosen at random to serve as the training set. The remaining 20 specimens were put through their paces as a test group. To determine a connection between the sub-grain cellular structure of SiCs/AlSi20Mg nanocomposites and their mechanical properties, KNN (K-Nearest Neighbors), AdaBoost, decision trees, gradient tree, and extra trees boosting regressions were all employed as machine learning methods.

ML techniques

The value was used as the performance parameter for a regressor trained with machine learning. This is because the root mean square error (RMSE) is further complex to outliers than the root square of the MSE (mean square error), where the impact of error is proportionate to its magnitude. Errors are also evaluated relative to one another [27]:

$$RMSE = \sqrt{\frac{T_{i=1}\left(y_t - \hat{y}_t\right)^2}{N}} \quad (5)$$

$$MSE = \frac{T}{N}\sum_{i=1}^{N}\left(y_t - \hat{y}_t\right)^2 \quad (6)$$

Where $\hat{y}_t$ is forecasting of a regression depending on variable y_t, N is no data.

Mean normalization was applied to the feature values with:

$$\overline{X} = \frac{X - average(X)}{stdev(X)} \quad (7)$$

A variety of regressors based on machine learning were applied here. AdaBoost is ameta-estimator that first uses the input dataset to fit a regressor and then uses the same dataset to provide more copies of the regressor with weights of instances changed based on the prediction error [28]. With Gradient Tree Boosting, an additional model is constructed in an incremental, forward fashion [29]. It enables the optimization of non-trivial loss functions that can be differentiated. Each iteration involves fitting a regression tree to the negative gradient of a based on the functional loss. The input for K-neighbors neural network is the k nearest training instances from the data collection, while the method's outcome is the object's property value. The mean of the predicted values of KNN is used [30]. The prediction value is deduced from the input data x and the number K.

$$\hat{y}_t = \left(\frac{1}{K}\right)\sum_{x_{1<N_k(x)}} y_i$$

Where, $N_k(x)$ is the K nearest neighbor points to the input x, y_i represents the output value for each x_i in $N_k(x)$.

Using either the Euclidean or Mahalanob is distance, KNN regression determines how similar the query example is to the labeled instances. Then, using RMSE and cross-validation, the labeled examples at increasing distances determine the best possible value for K, the number of nearest neighbors.

Learning fundamental decision rules from the properties of the data is the purpose of utilizing decisional trees to construct a model that assesses the target rate. A tree's inner nodes stand for attributes to be tested, its branches for test results, and its leaf nodes for class labels. While gradually building a decision tree, it breaks down a dataset into ever-smaller pieces [31]. Regarding machine learning, Extra Trees takes a top-down approach to growing a forest of unpruned trees [32]. When constructing its trees, Extra Trees fully uses all available training data. Before beginning the procedure, m structures are chosen randomly as split elements for each network node. The dividing lines between each feature group are likewise chosen at random. Selecting features and thresholds at random will significantly increase the randomness of the process, which will further reduce the variance [33, 34]. The minimal number of samples on the leaf nodes, the sum of arbitrarily picked features, and the number of trees are three crucial hyperparameters that need to be modified. When added to decision forests algorithms, Extra Trees, also known as severely randomized trees, add random elements. It uses a meta-estimator to increase predicted accuracy and regulate overfitting by fitting multiple randomized decision trees to different dataset subsamples and

averaging the results. Collectively, these classifiers can make a more accurate forecastthan anyone could do alone. A typical Extra Trees approximation is depicted in (8):

$$\hat{y}(x) = \sum_{i_1=0}^{N} \ldots\ldots \sum_{i_1=0}^{N} I_{(i_1 \ldots i_n)}(x) \sum X \in (X_1, \ldots . X_n) \lambda^{X}_{(i_1, \ldots, i_n)} \prod X_1 \in X^{x_i} \quad (8)$$

Where N is specimen size, $I(i_1,\ldots,i_n)(x)$ is the characteristic function of the hyper-interval, and $\lambda^{X}_{(i_1,\ldots,i_n)}$ is real-values parameters depend on input xi and output y_i of the algorithm.

By projecting each feature onto many principal components, this study uses principal component analysis to reduce the dimensionality of the structures while keeping as much of the data's original variance as probable. Investigating the hidden connections throughout massive datasets is its primary function. The core notion behind principal components analysis is choosing K (here, K = 3, which means we've selected units of the orthogonal basis on three data dimensions). By transforming the actual data to these 3 sets of bases, researcher can eliminate the covariance between any two features and increase the variancebetween elements. The same information that would have required 83 elements in the original interplanetary can be conveyed with just 3 extra components for dimensionality reduction.

Results and Discussion

Characterization of nanocomposite and cellular framework

AlSi20Mg powders have SiCs deposited on their surfaces after being ball milled. Thesurface of the ball-milled nanocomposites has a composition of Al-67.8 wt.%, C-25.3%, Si-6.6%, and Mg-0.34 wt.%, as shown in the elemental distribution mapping in figure 5. Afterball milling, the carbon element map shows that the SiCs are evenly distributed across thesurfaces of the AlSi20Mg powder, a necessary step for the SLM of homogeneity and density of SiCs/AlSi20Mg nanocomposites.

Figure 6 displays a computer-aided design representation of a tensile bar testing. Thestandard yield strength was 380 x 14. Scratched nanocomposite samples were incised to expose the melt pool's morphology [35]. Crack fronts relative to the melt pool structure aredisplayed in figure 7. The high aspect ratio structure along the fracture front in the melt pool is now clearly apparent due to the tensile strength. In addition, the SiC phase is visiblein the nanocomposites. Figure 7a and 7b depict two distinct fracture propagation routes,one caused by melt pool borders and the other by an elongated melt pool structure. When a crack is localized to the central areas of a melt pool, the cellular network is the primary barrier to crack propagation, as discovered by the author [36]. It provides further evidencethat the mechanical properties of AlSi20Mg-based composites are related to their cellular structure's sub-grain size. Fractographic images of SiC/AlSi20Mg nanocomposites undertensile stress are displayed in figure 8. This material exhibited ductile fracture with dimple rupture patterns.

The results demonstrated that the suggested framework is reliable and could accurately describe the form and magnitude information of the well-fine and HAZ coarse cellular zone

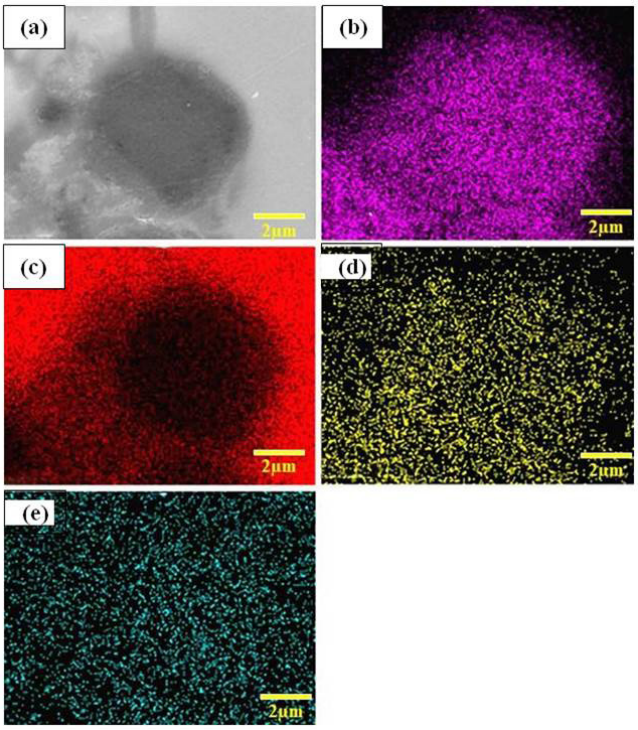


Figure 5: Ball-milled SiC/AlSi20Mg nanocomposite powders containing 0.5 wt.% SiC, as shown by **(a)** SEM. The elemental distribution **(b)** Aluminium, **(c)** Silicon, **(d)** Magnesium, and **(e)** Copper on the material surfaces as revealed by energy dispersive X-ray spectra mapping.

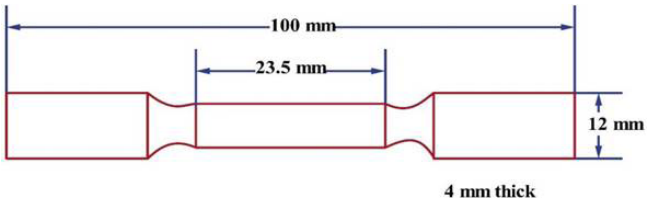


Figure 6: A computer-aided design representation of a tensile bar.

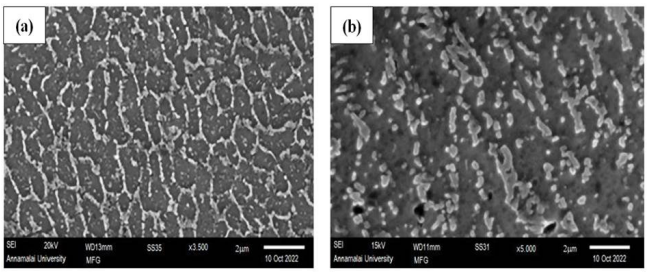


Figure 7: The morphology of the melt pool at the crack front during the tensile test reveals **(a)** the deviations in the route of crack propagation generated by the borders of the melt pool and **(b)** the extended melt pool pattern.

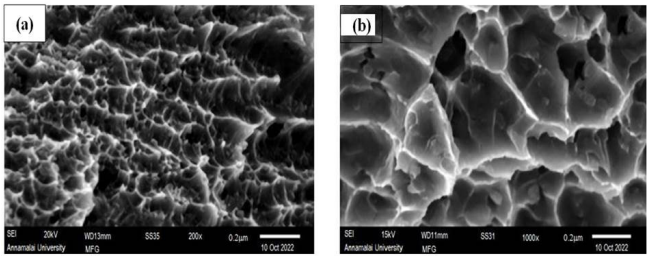


Figure 8: Tensile sample fractographic image of SiC/AlSi20Mg nanocomposite with magnification of **(a)** 200X and **(b)** 1000X.

Table 2: Median cell property range in the HAZ and fine cell zone.

Features	HAZ	Fine cell zone
Eccentricity	0.87	0.82
Euler number	0.98	0.97
Form factor	0.52	0.58
Perimeter (μm)	3.281	2.886
Minimum axis length (μm)	0.455	0.427
Extent	0.63	0.66
Solidity	0.88	0.92
Maximum axis length (μm)	0.728	0.723
Area (μm²)	17.12	13.26
Compactness	2.82	2.44

of SiC/AlSi20Mg composites. Table 2 displays the average values for each attribute. However, the fine cellular structure of the SiC/AlSi20Mg nanocomposites constitutes the dominant phase. Therefore, only the delicate cellular zonesare examined here, along with their connections to mechanical qualities like hardness thenrelative density.

Predicting relationships between microstructure and properties using ML

The SiC/AlSi20Mg nanocomposites hardness and relative mass density were predicted using a set of 83 attributes generated from the sub-grain cell separation structureand analyzed using KNN, Gradient Boost, decision trees, AdaBoost, and Extra Trees. A normalization procedure was applied to each feature to eliminate any inherent bias. A validation set comprised of the remaining 20 SEM pictures was utilized to evaluate the model's accuracy.

It was determined which features were most important using a combination of AdaBoost, a decision tree, and the Extra Trees regression (Figure 9). AdaBoost was proven tobe most effective at evaluating the hardness of SiC/AlSi20Mg nanocomposites based on the following 5 criteria: Zernike moment (9.98%), perimeter (9.14%), eccentricity (8.13%), compact (7.56%), and maximal radius (7.23%). The decision tree regressor uses the following 5 features: eccentricity (34.18%), mean radius (29.34%), extension (18.26%), orientation (9.12 %), and form factor (3.1%). The top 5 most important features for Extra Trees are the Zernike moment (9.98%), Zernike moment (9.98%), eccentricity (9.23%), form factor (8.14%), and compactness (7.56%), proving that the aspiration of the sub-grain cellular outline and dimension is critical to the mechanical characteristics of the SiC/AlSi20Mg composites. Eccentricity is a key factor that will playa role in defining the mechanical attributes of the future.

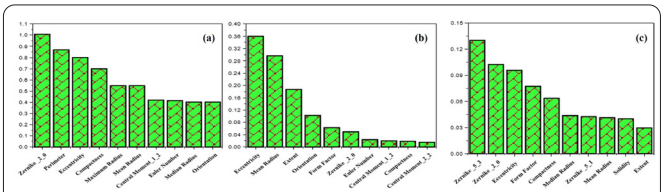


Figure 9: Hardness prediction of SiC/AlSi20Mg nanocomposites using **(a)** AdaBoost, **(b)** Extra trees, and **(c)** Decision tree in order of significance of features.

Hardness and relative mass density data for SiC/AlSi20Mg nanocomposites were compared to the model predictions. Figure 9 shows that the predicted hardness values veryclose to the actual values. Measures of machine learning algorithms' effectiveness are tabulated in table 3. AdaBoost's RMSE is 6.264 HV, MSE is 36.129 HV², and RE is 3.17%, making it the most accurate prediction method. The RMSE, MSE, and RE for Extra Trees prediction performance are 9.328 HV, 71.643 HV², and 6.12%, respectively. Sub-grain cellular structure is directly related to the mechanical properties of SiC/AlSi20Mg nanocomposites, as even the weakest ML algorithm in this work can produce a RE of 6.12%. The decision tree technique may predict the relative mass density with the highestaccuracy, which has an RMSE of 3.12%, an MSE of 0.0612%, and a RE of 1.61. Its prediction performance is superior to other base learners (Table 4).

The central feature values for the high hardness specimen are 0.76 for eccentricity, 3.56 pixels for mean radius, 5.47 for compactness, 2.65 μm for perimeter, 0.46 for extension, and 0.16 for Zernike 2_0 (Figure 10). For a given mean radius, a more compact shape and smaller perimeter will produce a more rigid surface. These findings demonstrate the proposed model's ability to accurately predict mechanical properties from inputs consistingof sub-grain cellular details. This finding demonstrates that the model created here may yield relatively accurate results even when working with a small training set.

Table 3: Comparing the efficacy of several ML techniques for predicting surface hardness.

MImethod	RMSE (HV)	MSE (HV²)	RE (%)
AdaBoost	6.264	36.129	3.17
Gradient Boost	8.242	51.913	4.23
KNN	8.598	59.326	5.41
Decision trees	9.546	73.724	5.63
Extra Trees	9.328	71.643	6.12

Table 4: Comparing the efficacy of several ML techniques for predicting the relative mass density.

MImethod	RMSE (HV)	MSE (HV²)	RE (%)
KNN	2.08	0.0597	1.89
Gradient Boost	2.11	0.0605	1.87
Decision trees	3.12	0.0612	1.61
AdaBoost	3.06	0.0595	1.98
Extra Trees	3.01	0.04523	1.75

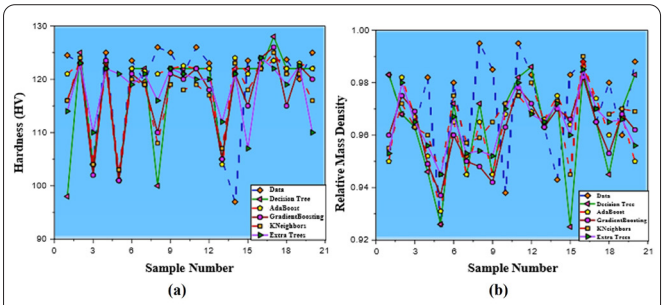


Figure 10: Predicting the **(a)** hardness and **(b)** relative mass density of SiC/AlSi20Mg composites utilizing sub-grain cellular structure characteristics and several ML algorithms.

Microstructure-property relationship prediction using PCA

To normalize the higher dimensional characteristics dataset (83 structures in our instance) with linked parameters, PCA employs a collection of linearly uncorrelated vectors to define the differences between the features. For this study, researcher uses the first three principal components to analyze the primary variances of the observations, therefore decreasing the dimensionality of the featuredatasets (PC1, PC2, and PC3).

Hardness and relative mass density measurements of SiC/AlSi20Mg nanocomposites are reported, together with PCA model results. The impact of PCA decomposition on hardness prediction accuracy is shown in figure 11 and table 5. After PCA decomposition, Extra Tress from AdaBoost becomes the most effective ML algorithm. Reduced from 5.941 HV to 6.426 HV; increased from35.245 HV^2 to 39.912 HV^2; and increased from 2.51% to 3.73% was the original RMSE, MSE, and RE, respectively. While PCA dimensional reduction can reduce prediction accuracy, it dramatically simplifies SEM image data registration, especially when dealingwith moderate to large datasets.

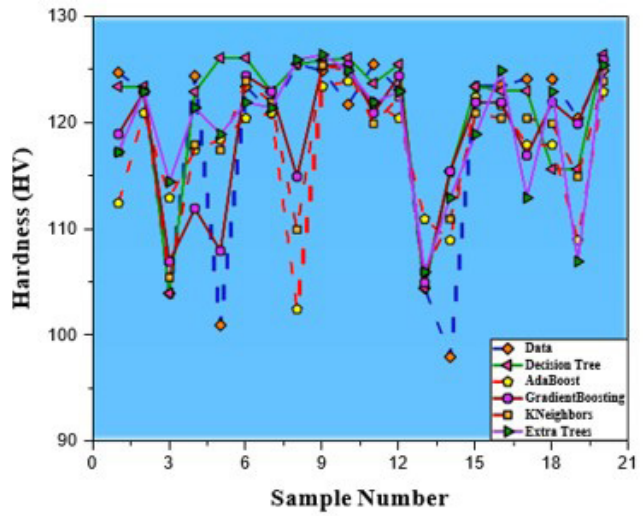


Figure 11: Variable ML approaches employing PCA decomposition to forecast the hardness of SiC/AlSi20Mg nanocomposites.

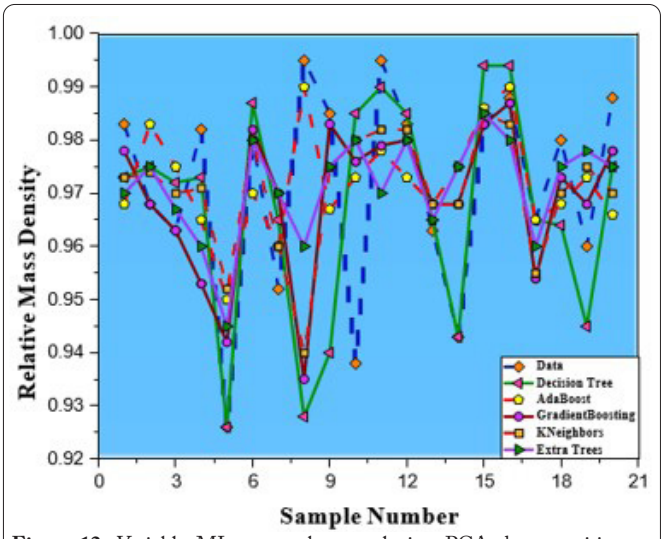


Figure 12: Variable ML approaches employing PCA decomposition to forecast the relative mass density of SiC/AlSi20Mg nanocomposites.

Figure 12 and table 6 depict the results of PCA relative mass density prediction. After PCA decomposition, the top-performing algorithm shifts from decision trees to AdaBoost. The initial RMSE was 2.41%, the MSE was 0.058%, and the RE was 1.59%; these were all reduced to 1.82%, 0.032%, and 1.53%, respectively. With the use of PCA, researcher can better estimate relative mass density since the PCA disintegration preserves the foremost shape and geometrical data of the primary properties.

Table 5: Analyzing the efficacy of several ML approaches employing PCA decompositionfeatures for surface hardness prediction.

MItechniques	RMSE (HV)	MSE (HV^2)	RE (%)
KNN	6.746	43.921	4.22
Gradient Boost	7.627	57.563	4.85
Decision trees	7.459	54.496	3.63
AdaBoost	8.712	74.995	5.83
Extra Trees	6.426	39.912	3.73

Table 6: Analyzing the efficacy of several ML techniques that utilize PCA decompositioncharacteristics to predict the relative mass density.

MItechniques	RMSE (HV)	MSE (HV^2)	RE (%)
KNN	1.96	0.0362	1.56
Decision trees	2.75	0.0718	1.73
Gradient Boost	2.12	0.0449	1.57
AdaBoost	1.82	0.0326	1.53
Extra Trees	2.19	0.0393	1.64

Conclusions

The fabrication of SiC-reinforced AA2219 was accomplished with various laser powers and scanning rates. Laser melting was used to investigate the distinctive cellular microstructures of Al-Si eutectics and the densification behavior of these materials.

A segmentation framework for cellular structures was presented to get at the geometric characteristics of cells. Using ML, the relationships between microstructure and properties were investigated, leading to highly accurate hardness and relative mass density predictions. In this and related investigations, the microstructure-property connections of PFB-produced AlSi20Mg-based composites are being explored for the first time. Following is a brief synopsis of the study's key results:

- The stretching of the melt pool pattern at the crack front of the cracked tensile specimen resulted in a microstructure with a high aspect ratio. They found that the nanocomposites have a SiC phase. Variations in crack propagation paths caused by melt pool borders and the cell structure of the material operate as the principal barrierto fracture formation.
- A significant link was discovered between the nanocomposites' mechanical propertiesand their cellular structure sub-grain size. The dimensions and geometry of

a eutecticsub-cell change for different values of the laser parameters. All three measures of cellsize (area, perimeter, and length) are more significant for cells in the coarse cellular zone than those in the fine cellular zone.

- Image inversion, cell nuclei search, and cell creation were all crucial steps in properlysegmenting cells in the cellular zone. Overall, SiC/AlSi20Mg nanocomposites contained 83 geometric features per cell across the fine and coarse cell zones. The mechanical characteristics of a nanocomposite sample may be predicted using just four microstructural characteristics: the perimeter, mean radius, eccentricity, and the Zernike moment 2_0.
- Predictions of mechanical properties of SiC/ AlSi20Mg nanocomposites were successful using ML algorithms such as Extra Trees regressors, KNN, decision tree, gradient tree boosting, and AdaBoost, which all correlated mechanical characteristics with geometrical characteristics of cellular zone. The hardness and the relative mass density may be predicted using PCAs, with an inaccuracy of 3.73 and 1.53%, respectively.

Acknowledgements

None.

Conflict of Interest

None.

References

1. Chen R, Bratten A, Rittenhouse J, Huang T, Jia W, et al. 2022. Additive manufacturing of complexly shaped SiC with high density via extrusion-based technique–effects of slurry thixotropic behavior and 3D printing parameters. *Ceram Int* 48(19): 28444-28454. https://doi.org/10.1016/j.ceramint.2022.06.158
2. Xue T, Chen L, Zhang Z, Zhao J, Zhang Y, et al. 2022. Data-driven analysis in magnetic field-assisted electrical discharge machining of high-volume SiC_p/Al. *Int J Adv Manuf Technol* 122(5-6): 2775-2791. https://doi.org/10.1007/s00170-022-09940-4
3. Twardowski P, Tabaszewski M, Wiciak-Pikuła M, Felusiak-Czyryca A. 2021. Identification of tool wear using acoustic emission signal and machine learning methods. *Precis Eng* 72: 738-744. https://doi.org/10.1016/j.precisioneng.2021.07.019
4. Kordijazi A, Behera S, Patel D, Rohatgi P, Nosonovsky M. 2021. Predictive analysis of wettability of Al-Si based multiphase alloys and aluminum matrix composites by machine learning and physical modeling. *Langmuir* 37(12): 3766-3777. https://doi.org/10.1021/acs.langmuir.1c00358
5. Thankachan T, Prakash KS, Malini R, Ramu S, Sundararaj P, et al. 2019. Prediction of surface roughness and material removal rate in wire electrical discharge machining on aluminum based alloys/composites using Taguchi coupled Grey Relational Analysis and Artificial Neural Networks. *Appl Surf Sci* 472: 22-35. https://doi.org/10.1016/j.apsusc.2018.06.117
6. Hasan MS, Kordijazi A, Rohatgi PK, Nosonovsky M. 2022. Triboinformatics approach for friction and wear prediction of Al-graphite composites using machine learning methods. *J Tribol* 144(1): 011701. https://doi.org/10.1115/1.4050525
7. Yang Z, Yang M, Sisson R, Li Y, Liang J. 2022. A machine-learning model to predict tensile properties of Ti6Al4V parts prepared by laser powder bed fusion with hot isostatic pressing. *Mater Today Commun* 33: 104205. https://doi.org/10.1016/j.mtcomm.2022.104205
8. Yadav P, Rigo O, Arvieu C, Singh VK, Lacoste E. 2022. Data processing techniques for *in-situ* monitoring in L-PBF process. *J Manuf Process* 81: 155-165. https://doi.org/10.1016/j.jmapro.2022.06.062
9. He P, Liu Q, Kruzic JJ, Li X. 2022. Machine-learning assisted additive manufacturing of a TiCN reinforced AlSi10Mg composite with tailorable mechanical properties. *Mater Lett* 307: 131018. https://doi.org/10.1016/j.matlet.2021.131018
10. Rahman MS, Ciaccio J, Chakravarty UK. 2021. A machine learning approach for predicting melt-pool dynamics of Ti-6Al-4V alloy in the laser powder-bed fusion process. In ASME International Mechanical Engineering Congress and Exposition, American Society of Mechanical Engineers.
11. Yang L, Özel T. 2021. Physics-based simulation models for digital twin development in laser powder bed fusion. *Int J Mech Manuf Syst* 14(2): 143-163. https://doi.org/10.1504/IJMMS.2021.119155
12. Muhammad W, Brahme AP, Ibragimova O, Kang J, Inal K. 2021. A machine learning framework to predict local strain distribution and the evolution of plastic anisotropy & fracture in additively manufactured alloys. *Int J Plast* 136: 102867. https://doi.org/10.1016/j.ijplas.2020.102867
13. Paulson NH, Gould B, Wolff SJ, Stan M, Greco AC. 2020. Correlations between thermal history and keyhole porosity in laser powder bed fusion. *Addit Manuf* 34: 101213. https://doi.org/10.1016/j.addma.2020.101213
14. Doyle AC, Egan DS, Ryan CM, Parnell AC, Dowling DP. 2021. Application of the STRAY statistical learning algorithm for the evaluation of *in-situ* process monitoring data during L-PBF additive manufacturing. *Procedia Manuf* 54: 250-256. https://doi.org/10.1016/j.promfg.2021.07.039
15. Imani F, Gaikwad A, Montazeri M, Rao P, Yang H, et al. 2018. Process mapping and in-process monitoring of porosity in laser powder bed fusion using layerwise optical imaging. *J Manuf Sci Eng* 140(10): 101009. https://doi.org/10.1115/1.4040615
16. Yu T, Mo X, Chen M, Yao C. 2021. Machine-learning-assisted microstructure–property linkages of carbon nanotube-reinforced aluminum matrix nanocomposites produced by laser powder bed fusion. *Nanotechnol Rev* 10(1): 1410-1424. https://doi.org/10.1515/ntrev-2021-0093
17. Suzuki A, Shiba Y, Ibe H, Takata N, Kobashi M. 2022. Machine-learning assisted optimization of process parameters for controlling the microstructure in a laser powder bed fused WC/Co cemented carbide. *Addit Manuf* 59: 103089. https://doi.org/10.1016/j.addma.2022.103089
18. Li H, Zhao W, Li R, Liu Y. 2022. Progress on additive manufacturing of maraging steel. *Zhongguo Jiguang Chinese J Lasers* 49(1): 1402102. https://doi.org/10.3788/CJL202249.1402102
19. Maleki E, Bagherifard S, Razavi N, Bandini M, du Plessis A, et al. 2022. On the efficiency of machine learning for fatigue assessment of post-processed additively manufactured AlSi10Mg. *Int J Fatigue* 160: 106841. https://doi.org/10.1016/j.ijfatigue.2022.106841
20. Snider-Simon B, Frantziskonis G. 2022. Development of statistical models for porosity from digital optical micrographs with application to metal additive manufacturing microstructure. *Comput Mater Sci* 203: 111128. https://doi.org/10.1016/j.commatsci.2021.111128
21. Elangeswaran C, Cutolo A, Gallas S, Dinh TD, Lammens N, et al. 2022. Predicting fatigue life of metal LPBF components by combining a large fatigue database for different sample conditions with novel simulation strategies. *Addit Manuf* 50: 102570. https://doi.org/10.1016/j.addma.2021.102570
22. Sofinowski K, Wittwer M, Seita M. 2022. Encoding data into metal alloys using laser powder bed fusion. *Addit Manuf* 52: 102683. https://doi.org/10.1016/j.addma.2022.102683
23. Sanchez S, Rengasamy D, Hyde CJ, Figueredo GP, Rothwell B. 2021. Machine learning to determine the main factors affecting creep rates in laser powder bed fusion. *J Intell Manuf* 32(8): 2353-2373. https://doi.org/10.1007/s10845-021-01785-0

24. Lesko CC, Sheridan LC, Gockel JE. 2021. Microhardness as a function of process parameters in additively manufactured alloy 718. *J Mater Eng Perform* 30(9): 6630-6639. https://doi.org/10.1007/s11665-021-05938-3

25. Li Y, Li Z, Lai WJ, Xu H, Xue Z, et al. 2021. Machine Learning based parameter calibration for multi-scale material modeling of laser powder bed fusion (L-PBF) AlSi10Mg. *SAE Int J Adv Curr Pract Mobility* 3(4): 1526-1534. https://doi.org/10.4271/2021-01-0309

26. Dovgyy B, Simonelli M, Pham MS. 2021. Alloy design against the solidification cracking in fusion additive manufacturing: an application to a FeCrAl alloy. *Mater Res Lett* 9(8): 350-357. https://doi.org/10.1080/21663831.2021.1922945

27. Li H. 2020. Machine-learning based modelling for AM processes. In IEEE 10th International Conference Nanomaterials: Applications and Properties, Sumy, Ukraine.

28. Bhuvaneswari V, Rajeshkumar L, Saravanakumar R, Balaji D. 2022. Synthesis and characterization of bioceramics reinforced aluminium matrix composites. *Arch Metall Mater* 67(4): 1217-1226. https://doi.org/10.24425/amm.2022.141045

29. Arumugam P, Rajkumar S, Maridurai T, Mageshkumar K, Subbiah R, et al. 2022. Comparison of boron nitride (BN) reinforced sintered and extruded AA2219 nano-hybrid composite particle size effects on mechanical and metallurgical characteristics. *Mater Today Proc* 59: 1434-1437. https://doi.org/10.1016/j.matpr.2021.12.130

30. Rathore S, Singh RKR, Khan KLA. 2021. Effect of process parameters on mechanical properties of aluminum composite foam developed by friction stir processing. *Proc Inst Mech Eng Part B J Eng Manuf* 235(12): 1892-1903. https://doi.org/10.1177/09544054211021341

31. Kumar LR, Saravanakumar A, Bhuvaneswari V, Raja NK, Karthi P. 2020. Tribological behaviour of AA2219/MOS_2 metal matrix composites under lubrication. *AIP Conf Proc* 2207(1): 020005. https://doi.org/10.1063/5.0000042

32. Sangeethkumar E, Jaikumar M, Sridath KMN, Ramanathan V, Sathyamurthy R. 2019. Tribological study on hybrid metal matrix composites for application in automotive sector. *Mater Res Express* 6(5): 055703. https://doi.org/10.1088/2053-1591/ab0579

33. Renish RR, Pranesh MA, Karthik K, Vanarasi V. 2019. Experimental Investigation of Wear and Hardness Test Over AA2219 with Reinforcement of Tungsten Carbide. In Chandrasekhar U, Yang LJ, Gowthaman S (eds) Innovative Design, Analysis and Development Practices in Aerospace and Automotive Engineering. Lecture Notes in Mechanical Engineering. Springer, Singapore, pp 159-165.

34. Kumar BA, Krishnan MM, Sahayaraj AF, Refaai MRA, Yuvaraj G, et al. 2022. Characterization of the aluminium matrix composite reinforced with silicon nitride (AA6061/Si_3N_4) synthesized by the stir casting route. *Adv Mater Sci Eng* 2022: 8761865. https://doi.org/10.1155/2022/8761865

35. Saravanakumar A, Sivalingam S. 2018. Dry sliding wear of AA2219/Gr metal matrix composites. *Mater Today Proc* 5(2): 8321-8327. https://doi.org/10.1016/j.matpr.2017.11.524

36. Verma P, Pandian SM. 2021. Bionic effects of nano hydroxyapatite dentifrice on demineralised surface of enamel post orthodontic debonding: *in-vivo* split mouth study. *Prog Orthod* 22: 1-8. https://doi.org/10.1186/s40510-021-00381-5